

# **JGR** Solid Earth

### **RESEARCH ARTICLE**

10.1029/2019JB017985

#### **Key Points:**

- We derive a new viscoacoustic wave equation that enables frequency-independent quality factor
- This new equation is favored for having simplified fractional Laplacians and incorporating attenuation heterogeneity
- This proposed equation directly benefits seismic modeling and imaging applications

#### Correspondence to:

G. Xing, guangchi.xing@psu.edu

#### Citation:

Xing, G., & Zhu, T. (2019). Modeling frequency-independent Q viscoacoustic wave propagation in heterogeneous media. *Journal of Geophysical Research: Solid Earth*, 124, 11,568–11,584. https://doi.org/10. 1029/2019JB017985

Received 7 MAY 2019 Accepted 2 OCT 2019 Accepted article online 18 OCT 2019 Published online 13 NOV 2019

# Modeling Frequency-Independent *Q* Viscoacoustic Wave Propagation in Heterogeneous Media

Guangchi Xing<sup>1</sup> and Tieyuan Zhu<sup>1,2</sup>

<sup>1</sup>Department of Geosciences, Pennsylvania State University, University Park, PA, USA, <sup>2</sup>EMS Energy Institute, Pennsylvania State University, University Park, PA, USA

**Abstract** Quantifying the attenuation of seismic waves propagating in the Earth interior is critical to study the subsurface structure. Previous studies have proposed fractional anelastic wave equations to model the frequency-independent Q seismic wave propagation. Such wave equations involve fractional derivatives that pose computational challenges for the numerical schemes in terms of accuracy and efficiency when dealing with heterogeneous Earth media. To tackle these challenges, here we derive a new viscoacoustic wave equation, where the power terms of the fractional Laplacian operators are spatially independent, thus accurate and efficient methods (e.g., the Fourier pseudospectral method) can be adopted. Our derivation enables the resultant equation to capture both amplitude and phase signatures of the anelastic wave propagation by matching the complex wave numbers for all the frequencies of interest. We verify the derivation by comparing the dispersion curves of both the attenuation factor and the phase velocity produced by the new wave equation with their theoretical values as well as the Pierre Shale in situ measurements. Following that, we use a synthetic attenuating gas chimney model to demonstrate the attenuation effects on seismic waveforms and then construct the Q-compensated reverse time migration to undo these effects for seismic image enhancement. Finally, we find that our forward modeling results can characterize the spatiotemporal attenuation effects revealed in the Frio-II CO<sub>2</sub> injection time-lapse seismic monitoring data. We expect this proposed equation to be useful to quantify the attenuation in seismic data to push the resolution limits of seismic imaging and inversion.

#### 1. Introduction

The anelastic property of the Earth materials gives rise to the energy loss of the seismic waves, which is especially significant in the presence of fluids (e.g., Müller et al., 2010), high temperature (e.g., Peters et al., 2012; Romanowicz, 1995), or partial melt (e.g., Wiens et al., 2008). This loss results in seismic attenuation, which has a considerable impact on the seismic recordings. In particular, seismic attenuation has two associated effects on seismic waveforms, that is, the amplitude decay and the velocity dispersion. Hence, it is critical to incorporate them into the modeling of seismic wave propagation.

The quality factor Q is defined as  $2\pi$  times the ratio of the stored energy to the lost energy in a single cycle of deformation, so its inverse  $Q^{-1}$ , the dissipation factor, is used to quantify the strength of seismic attenuation. It has been shown that the Earth materials exhibit a nearly constant Q behavior over the seismic frequency band from lab experiments and field measurements (e.g., Knopoff, 1964; McDonal et al., 1958), although the frequency-dependent Q theory is supported by some other seismological observations (e.g., Adam et al., 2009; Borgomano et al., 2017; Molyneux & Schmitt, 2000; Sams et al., 1997). It is worth to note that the observations of frequency-dependent Q often refer to a broad frequency range while the frequency-independent Q is limited in a narrow range. In this sense, as shown in Sams et al. (1997) and Adam et al. (2009), the frequency-independent Q is practically useful in the seismological modeling and imaging applications. Hence, we only focus on the frequency-independent Q paradigm in this study.

The frequency-independent Q is naturally characterized by introducing the complex velocity (Aki & Richards, 2002) where Q is explicitly expressed. In this case, it is not difficult to model the viscoelastic/viscoacoustic wave propagation using the frequency domain wave equation (e.g., Operto et al., 2007; Štekl & Pratt, 1998). However, the resultant Helmholtz-type equation is computationally formidable, especially in 3-D problems, due to the huge memory requirement, which prevents the frequency domain algorithms from practical applications.

©2019. American Geophysical Union. All Rights Reserved.



In the time domain, by taking seismic attenuation into account, the stress is, according to the viscoelastic constitutive relation, represented by the convolution of relaxation function and strain rate rather than a simple multiplication of them in the lossless elastic case. As a result, the calculation of the current stress/strain status essentially requires the entire history of previous status, which is challenging for memory as well. Over the past few decades, the time domain methods have been explored by a number of studies, in which the memory problem has been alleviated to various extents. The state-of-the-art techniques can be categorized into two major groups.

One group is based upon a variety of physical (rheological) models that are used to phenomenologically represent the viscoelastic behavior of Earth materials. These models consist of springs and dashpots where the spring exhibits elastic response and the dashpot shows viscous property. For instance, the mechanical element models such as the Maxwell model, the Kelvin-Voigt model, and the standard linear solid (SLS) model belong to this category. A single mechanical element leads to frequency-dependent Q, whereas a distribution of such elements with various relaxation times can be superposed in parallel to approximately represent the constant Q behavior in a limited frequency band (Liu et al., 1976). In this class, the generalized standard linear solid (GSLS) and the generalized Maxwell body (GMB) are the most popular examples, and they are equivalent to each other (Moczo & Kristek, 2005) as both of them produce exponential relaxation functions. This exponential property enables introducing internal memory variables that satisfy first-order ordinary differential equations (e.g., Carcione et al., 1988; Emmerich & Korn, 1987; Robertsson et al., 1994) to avoid storing the stress/strain history for the convolution operation. These memory variables, however, require significant additional computing time and memory, especially in 3-D elastic problems (Zhu et al., 2013), although the computational burden could be partly reduced by the coarse-grained technique (e.g., Day, 1998;van Driel & Nissen-Meyer, 2014), which redistributes the memory variables over multiple node points to model the expected viscoelastic behavior in an average sense. Moreover, the implicit Q encoding by a set of relaxation parameters makes the inverse problem technically challenging (Fichtner & van Driel, 2014).

Another group of methods is based on a mathematical model derived to capture the analytical frequency-independent *Q* behavior (Kjartansson, 1979). This Kjartansson model gives rise to a power law relaxation function so the storage of wavefield variable history cannot be avoided. A pioneering study (Caputo, 1967) formulated the constitutive relation of this model as a fractional time derivative. Based on this, Carcione et al. (2002), Carcione (2008), and Zhu (2017) applied Grünwald-Letnikov approximation to model the viscoacoustic, viscoelastic, and viscoelastic-anisotropic wavefields, respectively. But this approximation still requires substantial memory space to store the truncated wavefield variable history. An alternative solution is proposed by Lu and Hanyga (2004), in which they converted the fractional time derivative into an infinite integral and approximated it using Laguerre quadrature. The quadrature variables, the amount of which is more than 35 in their study, satisfy first-order ordinary differential equations but require considerable additional computational resources as well.

To address the memory problem, a promising direction was proposed by Chen and Holm (2004), where the fractional time derivative is converted into fractional spatial derivative, that is, the fractional Laplacian operator. Later on, their wave equation is improved by Treeby and Cox (2010) by adding another fractional Laplacian term that accounts for phase dispersion to meet the causality requirement defined by Kramers-Kronig relations (Waters et al., 2005). Independently, Carcione (2010) introduced the fractional Laplacian operator to model the constant *Q* seismic wave propagation, where this operator was naturally solved by the Fourier pseudospectral method due to its nonlocal property.

Recently, Zhu and Harris (2014) have proposed an acoustic wave equation with decoupled fractional Laplacians:

$$\frac{1}{c(\mathbf{x})^2} \frac{\partial^2 p(\mathbf{x}, t)}{\partial t^2} = \eta(\mathbf{x})(-\nabla^2)^{\gamma(\mathbf{x})+1} p(\mathbf{x}, t) + \tau(\mathbf{x}) \frac{\partial}{\partial t} (-\nabla^2)^{\gamma(\mathbf{x})+1/2} p(\mathbf{x}, t), \tag{1}$$

where  $p(\mathbf{x},t)$  is the pressure wavefield;  $c(\mathbf{x})$  is the seismic velocity;  $\gamma(\mathbf{x}) = \frac{1}{\pi} \arctan(\frac{1}{Q(\mathbf{x})})$  is a dimensionless parameter roughly proportional to  $Q^{-1}$ ;  $\eta(\mathbf{x})$  and  $\tau(\mathbf{x})$  are parameters determined by the viscoelastic properties of the media. This wave equation is favored because of the use of the fractional Laplacians since numerically solving them neither stores previous wavefields nor introduces additional variables. In addition,



it is capable to separate the amplitude decay and the velocity dispersion attenuation effects. As demonstrated by previous studies (Guo et al., 2016; Sun et al., 2015, 2016; Yang & Zhu, 2018; Zhu, 2014; Zhu et al., 2014; Zhu & Sun, 2017), this separation feature is the key to construct the seismic imaging, which requires preserving the dispersion while reversing the dissipation for the wavefields. Moreover, this wave equation has been used as an engine in the waveform tomography (Shen & Zhu, 2015; Xue et al., 2017).

In equation (1), we note that the fractional Laplacians  $(-\nabla^2)^{\gamma(x)+1}$  and  $(-\nabla^2)^{\gamma(x)+1/2}$  contain spatially dependent power terms, which bring about difficulties to the numerical implementation. Zhu and Harris (2014) solved these two operators using the pseudospectral method with the simplification on the spatially dependent power terms by taking the average values. Such an implementation results in inaccuracy, especially in highly heterogeneous Q media. Efforts have been made by several subsequent studies to handle the varying Q: Sun et al. (2015) proposed a wave extrapolation scheme with low-rank approximation but it faces a dilemma between excessive Fourier transform operations and small time steps, both of which result in significant computational loads; Yao et al. (2016) used Hermite distributed approximating functional (HDAF) method, but it is computationally intensive for highly heterogeneous models; Chen et al. (2016) derived an ad hoc viscoacoustic wave equation with constant-order fractional Laplacians by a trial-and-error method yet the equations lack rigorous validation; Yang and Zhu (2018) proposed a complex-valued wave equation with fixed power fractional Laplacians, but it involves the complex wavefields at each time step.

In this study, we aim to derive a new viscoacoustic wave equation involving fractional Laplacian operators with spatially independent powers so as to deal with heterogeneous Q media accurately. Starting from the dispersion relation, our derivation seeks for an equation that matches the phase velocities and the attenuation factors of the Kjartansson constant Q model over the frequency band of interest. To do that, we conduct the Taylor analysis and optimize the coefficients of the viscoacoustic wave equation with a desired form that not only inherits the memory efficiency and the ability to decouple attenuation effects from equation (1) but also has spatially independent power terms of fractional Laplacians.

The paper is organized as follows. We start from a brief review of the Kjartansson frequency-independent *Q* model. Then we show the derivation of the new viscoacoustic wave equation followed by presenting its advantages, validating its accuracy, and illustrating its implementation. Next, we conduct several numerical experiments using models with different complexities to demonstrate the performance of the new equation. We also present its applications to reverse time migration (RTM) and time-lapse seismic monitoring. Finally, we discuss several variants of this wave equation to balance the trade-off between accuracy and efficiency.

# 2. Wave Equation With Fixed Power Laplacian Operator

#### 2.1. Kjartansson Frequency-Independent Q Model

The complex modulus representing the mathematical frequency-independent Q model is given by Kjartansson (1979):

$$M(\omega) = M_0 (\frac{i\omega}{\omega_0})^{2\gamma},\tag{2}$$

where  $\omega_0$  is the reference angular frequency and  $M_0$  is a real parameter with the dimension of bulk modulus. The quality factor Q can be defined as the ratio of the real and the imaginary parts of the complex modulus (Carcione, 2007). Thus, equation (2) leads to  $Q = \frac{Re\{M\}}{Im\{M\}} = (\tan(\pi\gamma))^{-1}$ , which is frequency-independent. We have  $0 < \gamma < 0.5$  for any positive value of Q.

The stress-strain constitutive relation is characterized by the complex modulus in the frequency domain. Combining it with the equation of motion, we have  $Mk^2 = \rho_0 \omega^2$ , where k is the complex wave number and  $\rho_0$  is the ambient density. So, we obtain the Kjartansson complex wave number:

$$k(\omega) = \sqrt{\frac{\rho_0}{M_0}} \omega_0^{\gamma} \omega^{1-\gamma} e^{i(-\frac{\pi \gamma}{2})} = \frac{1}{c} \omega_0^{\gamma} \omega^{1-\gamma} e^{i(-\frac{\pi \gamma}{2})}, \tag{3}$$

where  $c=\sqrt{\frac{M_0}{\rho_0}}=c_0\cos(\frac{\pi\gamma}{2})$  and  $c_0$  is the reference phase velocity defined at the reference frequency  $\omega_0$ . The real and imaginary parts of the complex wave number govern the two attenuation associated effects, that is, the velocity dispersion and amplitude decay, respectively. Quantitatively, the dispersion of the phase

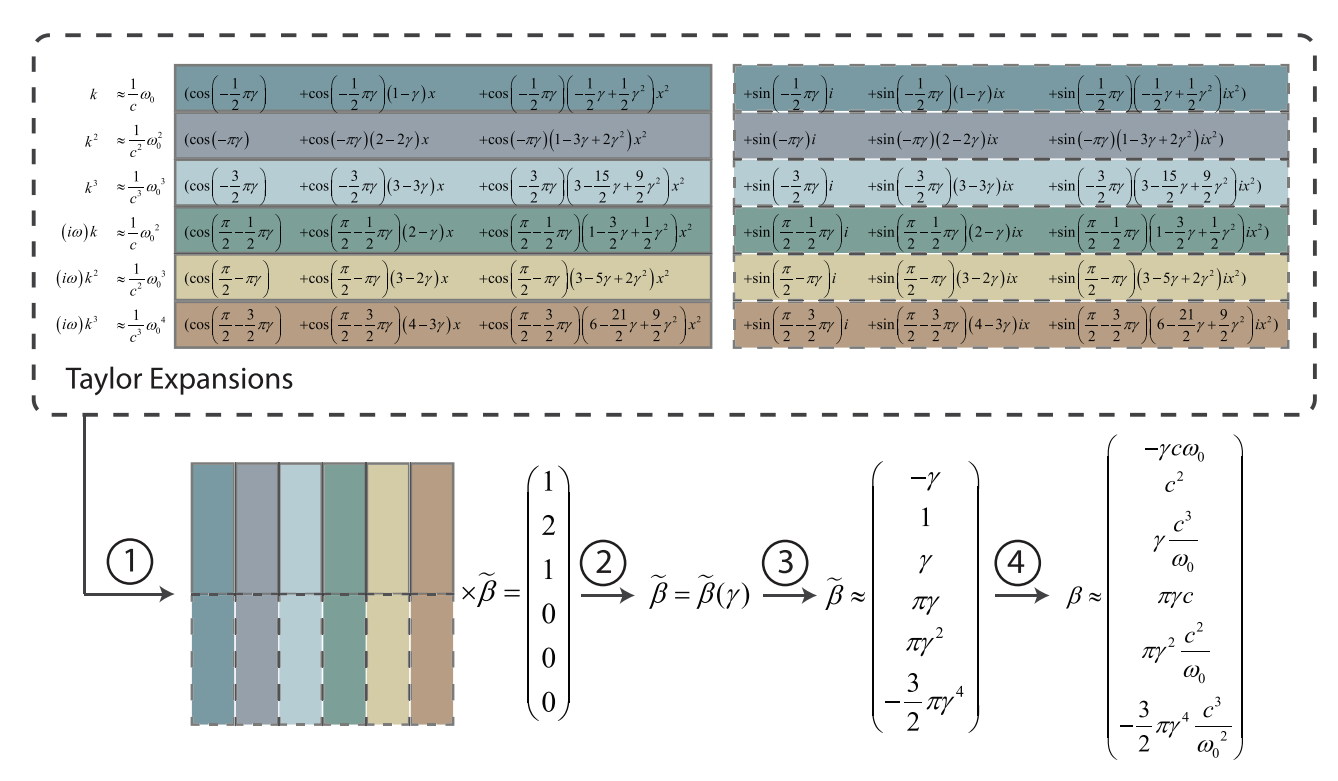


**Figure 1.** The workflow of the derivation process of the new viscoacoustic wave equation. We start from the Taylor expansions for each term of equation (6). Different colors indicate the coefficients of different terms, while the solid and dashed borders correspond to real and imaginary parts, respectively. The processes marked by numbers are as follows: (1) plug the Taylor expansion expressions into equation (6) and formulate the  $6 \times 6$  linear system problem; (2) analytically solve the linear system and obtain a complicated closed form representation of  $\tilde{\beta}$ , which is a function of  $\gamma$ ; (3) apply a second Taylor expansion with respect to  $\gamma$  and preserve the leading term; (4) convert the dimension-normalized parameters  $\tilde{\beta}$  back to  $\beta$ .

velocity  $c_p$  and the attenuation factor  $\alpha$  are expressed as

$$c_p(\omega) = \frac{\omega}{Re\{k\}} = c_0(\frac{\omega}{\omega_0})^{\gamma}$$
 (4)

$$\alpha(\omega) = -Im\{k\} = \frac{\omega}{c_0} (\frac{\omega}{\omega_0})^{-\gamma} \tan(\frac{\pi\gamma}{2}). \tag{5}$$

#### 2.2. Derivation of the Viscoacoustic Wave Equation

Our goal is to derive an approximate viscoacoustic wave equation that produces the Kjartansson complex wave number (equation (3)) so that both attenuation-associated effects are honored. In the meantime, we require that the spatial derivatives in the time-space domain equation only consists of fixed power (fractional) Laplacian operators so as to be effectively handled using the pseudospectral method (Carcione, 2010) or a special finite difference method (Duo et al., 2018). The Fourier transform of the fractional Laplacian is given by Chen and Holm (2004) as  $(-\nabla^2)^{\frac{e}{2}} \frac{F}{\hbar} k^e$ , while for time derivative we have  $\frac{\partial}{\partial t} \hat{k}^e$ . Hence, a tentative form of the frequency-wave number domain wave equation can meet the aforementioned requirements:

$$\omega^{2} = \beta_{1}k + \beta_{2}k^{2} + \beta_{3}k^{3} + \beta_{4}(i\omega)k + \beta_{5}(i\omega)k^{2} + \beta_{6}(i\omega)k^{3}, \tag{6}$$

where  $\beta_1,\beta_2,\ldots,\beta_6$  are real parameters related to media properties. The problem is converted to determining these parameters  $\beta=(\beta_1,\beta_2,\ldots,\beta_6)$  so that the solution of equation (6) approximates the wave number given in equation (3) for all the frequencies. Thus, we plug equation (3) into equation (6) and seek for appropriate parameters  $\beta$  to make the left- and right-hand sides equal. To do that, we apply a change of variable  $\omega=(1+x)\omega_0$  and conduct a Taylor analysis. By selecting a proper reference frequency for the calculation, for example, setting  $\omega_0=\frac{1}{2}(\omega_{\min}+\omega_{\max})$  to be the center for the frequency band of interest, we have  $-1\leq x\leq 1$ .

The workflow of the derivation process is shown in Figure 1. To make both sides approximately equal for all the frequencies, we match the coefficients of the real and imaginary parts of the leading terms including



 $x, x^2, x^3$  on both sides. This becomes a  $6 \times 6$  linear system problem. We then normalize the dimension of the unknown  $\beta$  by solving for  $\tilde{\beta} = (\frac{1}{c\omega_0}\beta_1, \frac{1}{c^2}\beta_2, \frac{\omega_0}{c^3}\beta_3, \frac{1}{c}\beta_4, \frac{\omega_0}{c^2}\beta_5, \frac{\omega_0^2}{c^3}\beta_6)$ .

The solution of this linear system is a complicated closed-form representation of  $\tilde{\beta}$ . To further reduce the complexity, we apply a second Taylor expansion for  $\tilde{\beta}$  in terms of  $\gamma$ . Taking advantage of symbolic computing (Meurer et al., 2017), which automatically simplifies expressions that are too complicated for manual manipulation into succinct forms, we obtain the clean form of  $\tilde{\beta}$  by preserving the leading term. So the resultant  $\beta$  is

$$(\beta_1, \beta_2, \beta_3, \beta_4, \beta_5, \beta_6) \approx (-\gamma c \omega_0, c^2, \gamma \frac{c^3}{\omega_0}, \pi \gamma c, \pi \gamma^2 \frac{c^2}{\omega_0}, -\frac{3}{2} \pi \gamma^4 \frac{c^3}{\omega_0^2}), \tag{7}$$

where the last term  $\beta_6$  can be safely omitted as it contains  $\gamma^4$ .

Substituting equation (7) into equation (6) followed by taking the inverse Fourier transform yields the time-space domain viscoacoustic wave equation:

$$\underbrace{\frac{1}{c^2} \frac{\partial^2 p}{\partial t^2} = \nabla^2 p}_{\text{Acoustic}} + \underbrace{(\gamma \frac{\omega_0}{c} (-\nabla^2)^{\frac{1}{2}} - \gamma \frac{c}{\omega_0} (-\nabla^2)^{\frac{3}{2}}) p}_{\text{Velocity Dispersion}} + \underbrace{(-\pi \gamma \frac{1}{c} (-\nabla^2)^{\frac{1}{2}} + \pi \gamma^2 \frac{1}{\omega_0} \nabla^2) \frac{\partial}{\partial t} p}_{\text{Amplitude Loss}}.$$
(8)

# 2.3. Advantages of the Viscoacoustic Wave Equation

Equation (8) can be interpreted as the nonattenuating acoustic wave equation plus two correction terms: the  $(-\nabla^2)^{\frac{1}{2}}p$  and  $(-\nabla^2)^{\frac{3}{2}}p$  term denotes velocity dispersion while the  $(-\nabla^2)^{\frac{1}{2}}\frac{\partial}{\partial t}p$  and  $\nabla^2\frac{\partial}{\partial t}p$  term corresponds to amplitude decay. Following Zhu (2014), we can obtain the dispersion-dominated wave equation by dropping the amplitude decay term:

$$\frac{1}{c^2} \frac{\partial^2 p}{\partial t^2} = \nabla^2 p + \left(\gamma \frac{\omega_0}{c} (-\nabla^2)^{\frac{1}{2}} - \gamma \frac{c}{\omega_0} (-\nabla^2)^{\frac{3}{2}}\right) p. \tag{9}$$

Similarly, only preserving the latter correction term lead to the loss-dominated wave equation:

$$\frac{1}{c^2} \frac{\partial^2 p}{\partial t^2} = \nabla^2 p + (-\pi \gamma \frac{1}{c} (-\nabla^2)^{\frac{1}{2}} + \pi \gamma^2 \frac{1}{\omega_0} \nabla^2) \frac{\partial}{\partial t} p. \tag{10}$$

This decoupling property has been showed to facilitate the implementation of the Q-compensated reverse time migration (e.g., Zhu, 2014; Zhu et al., 2014), which will be demonstrated in an example in section 3.3. Apparently, this wave equation reduces to the classical acoustic wave equation when the attenuation is ignorable ( $Q \to \infty$ ) since  $\beta_1, \beta_3, \beta_4, \beta_5 \to 0$  as  $\gamma \to 0$ . In addition, having the Q (or  $\gamma$ ) explicitly present in the coefficients of the equation would facilitate the formulation of the inverse problem (Fichtner & van Driel, 2014). In terms of the computational cost, this new wave equation avoids introducing the memory variables or storing the stress/strain history. Another important feature of this equation is that the power terms of the fractional Laplacian operators are independent of the model complexity so that it can accurately handle heterogeneous attenuation models.

#### 2.4. Validation of Dispersion Relations

We validate the approximate dispersion relations against the Pierre Shale attenuation measurements, which was extracted from seismic borehole data collected from the Pierre Shale in Eastern Colorado (McDonal et al., 1958; Wuenschel, 1965). Based on the measurements, we set the reference P wave velocity of the rock to be 2,131 m/s at 1,500 Hz with the density of 2,200 kg/m³ and a quality factor Q=32. Moreover, we consider the cases with large (Q=10) and small (Q=100) attenuation for a typical surface seismic frequency range (10–60 Hz) as well as a broader range (10–200 Hz). Given these media parameters, we select the midpoints of the frequency ranges, that is, 35 and 105 Hz, as the reference frequencies. Equation (6) is numerically solved for the complex wave number at different frequencies. The resultant phase velocities and attenuation factors are compared with the ones produced by theoretical solutions given in equations (4) and (5). As shown in Figure 2, the curves for both the attenuation factor and the phase velocity match well with the theoretical solutions. The velocity dispersion has some inaccuracy at the low-frequency component, especially for the broader band case (Figure 2c). It is not surprising that the fitting becomes better for higher Q (low attenuation).

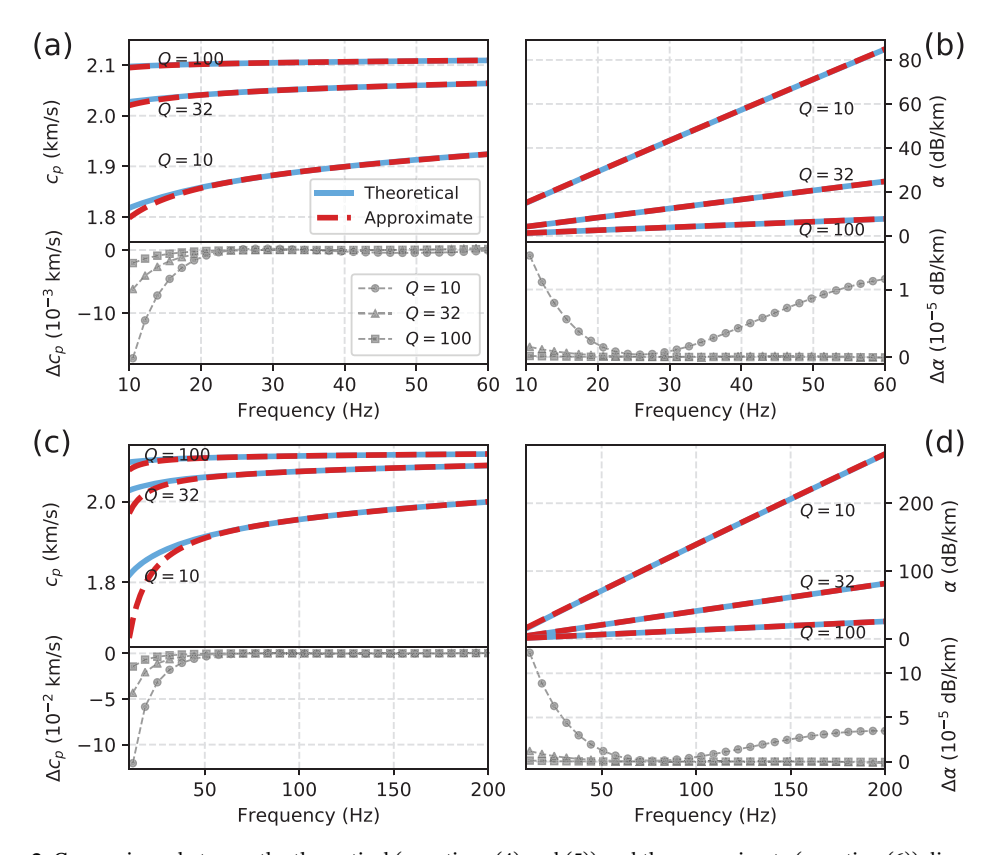


**Figure 2.** Comparisons between the theoretical (equations (4) and (5)) and the approximate (equation (6)) dispersion relations as well as their residuals. (a) Phase velocity for a narrow band with the reference frequency 35 Hz; (b) attenuation factor for a narrow band with the reference frequency 35 Hz; (c) phase velocity for a broad band with the reference frequency 105 Hz; (d) attenuation factor for a broad band with the reference frequency 105 Hz. Three cases with different quality factors are computed: Q = 10, Q = 32, and Q = 100. The legends of (a) also apply to (b), (c), and (d).

Then, we compare the theoretical and approximate dispersion relations with the Pierre Shale in situ data in Figure 3. To adapt the frequency range of the measurements, we consider a very broad band of 50–600 Hz and select the midpoint 325 Hz as the reference frequency. The comparisons (Figure 3) indicate that the approximate curves agree with the theoretical ones as well as the measurements, except for the phase velocity discrepancy at low frequencies as Figure 2. The possible reason is that the larger curvature of this frequency range is harder to be fitted by the third-order equation (6).

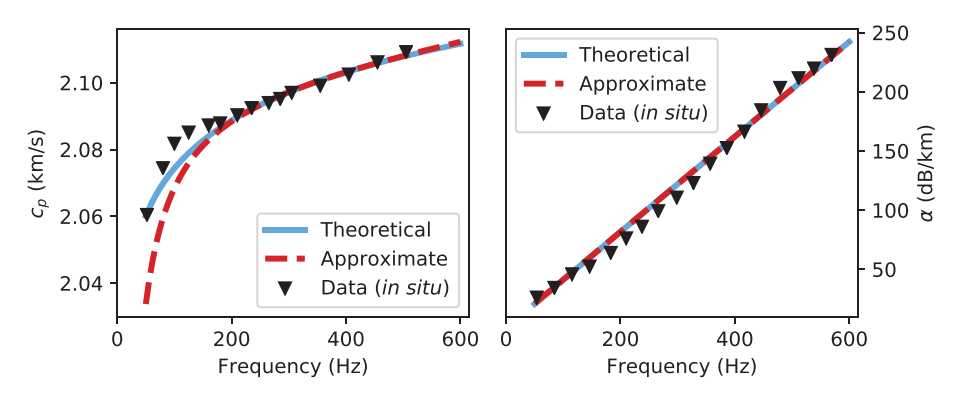


**Figure 3.** Comparisons between the theoretical (blue solid lines, equations (4) and (5)), approximate (red dashed lines, equation (6)) and in situ measured (black triangles) dispersion relations of the Pierre Shale for (left) phase velocity and (right) attenuation factor.

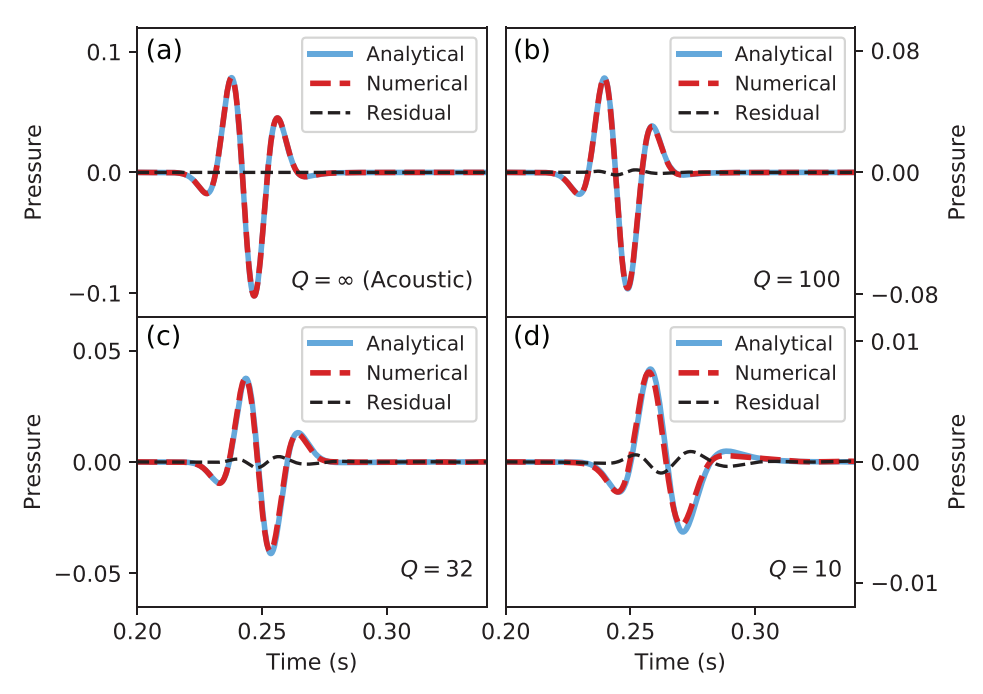


Figure 4. Comparison of the analytical (blue solid lines) and the numerical synthetic seismograms (red dashed lines) as well as their residuals (black dashed lines) in homogeneous media for (a)  $Q = \infty$  (acoustic); (b) Q = 100; (c) Q = 32, and (d) Q = 10.

# 2.5. Numerical Implementation

Numerically, we recast the second-order partial differential equation (8) into a series of coupled first-order equations (Treeby & Cox, 2010):

$$\frac{\partial \mathbf{u}}{\partial t} = -\frac{1}{\rho_0} \nabla p,\tag{11}$$

$$\frac{\partial \rho}{\partial t} = -\rho_0 \nabla \cdot \mathbf{u},\tag{12}$$

$$p = (\beta_1(-\nabla^2)^{-\frac{1}{2}} + \beta_2 + \beta_3(-\nabla^2)^{\frac{1}{2}})\rho - (\beta_4(-\nabla^2)^{-\frac{1}{2}} + \beta_5)\rho_0\nabla \cdot \mathbf{u} + s,$$
(13)

where  ${\bf u}$  is the particle velocity,  $\rho$  is the acoustic density, s is the pressure source, and  $\beta_1, \beta_2, \ldots, \beta_5$  are given by equation (7). Equations (11)–(13) thus correspond to momentum conservation, mass conservation, and pressure-density relation, respectively. Such manipulation improves the flexibility of incorporating density heterogeneity and the PML boundaries (Berenger, 1994).

The time derivatives are computed by the finite difference time marching scheme, while the spatial derivatives are implemented by the staggered-grid pseudospectral method (Carcione, 1999). In particular, the generalized Fourier method (Carcione, 2010) is used to evaluate fractional Laplacians  $(-\Delta^2)^{\epsilon} f(\mathbf{x}) = \mathcal{F}^{-1}\{k^{2\epsilon}\mathcal{F}\{f(\mathbf{x})\}\}$ , where  $\mathcal{F}$  and  $\mathcal{F}^{-1}$  are implemented by the forward and the inverse fast Fourier transform (FFT).

# 3. Numerical Examples

To evaluate the performance of the new viscoacoustic wave equation, we adopt equations (11)–(13) to generate synthetic seismograms for 2-D models with different levels of complexities. Then we construct the Q-compensated reverse time migration to enhance the seismic image and finally conduct a calibration test of modeled attenuation for the Frio-II  $\rm CO_2$  injection time-lapse monitoring model. For each experiment, we select the reference frequency to be the dominant frequency of the source wavelet; a constant density  $(2,200~\rm kg/m^3)$  is adopted unless otherwise specified.

# 3.1. Homogeneous Model

Following the Pierre Shale seismic parameters given in section 2.4, we study the attenuation effects on waveforms in a homogeneous model by testing different quality factors, that is, acoustic  $(Q = \infty)$ , Q = 100,

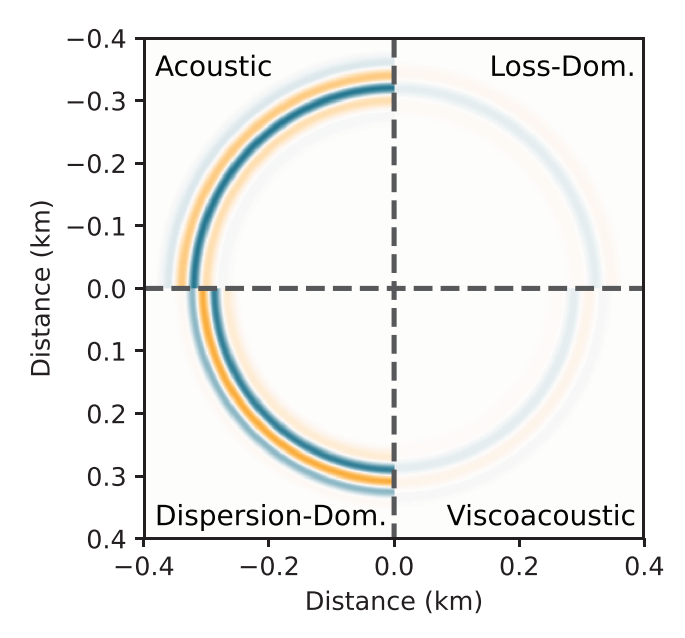


**Figure 5.** Wavefield snapshots at 210 ms for four simulations in homogeneous media. Each quadrant corresponds to a specific wave equation: acoustic, loss-dominated, dispersion-dominated, and viscoacoustic.

Q=32, and Q=10. The simulations are performed on a 2-D grid with a spacing of 2 m in both directions. A Ricker wavelet source with center frequency of 35 Hz is excited, and the response is recorded by a receiver with 400 m offset. The time step is 0.25 ms.

Figure 4 compares the numerical solutions with the analytical solutions obtained by convolving the source wavelet with the Green's functions (Carcione, 2007). We observe that as Q decreases, the peak amplitude becomes smaller while the waveform distorts more severely with comparison to the acoustic case. The numerical and analytical solutions agree with each other almost perfectly well for all simulations except for the low-Q case where the shapes of waveforms exhibit subtle differences, which might be caused by the inaccuracy in the phase velocity dispersion (Figure 2a).

To demonstrate the property of attenuation effects decoupling, we recompute the high-attenuation (Q=10) case on a square  $400\times400$  grid with the source located at the center of the model (400 m, 400 m). Four simulations are conducted using the acoustic, the loss-dominated (equation (10)), the dispersion-dominated (equation (9)), and the viscoacoustic wave equations (equation (8)), respectively. The wavefield snapshots at 210 ms for all the four simulations are shown in Figure 5. As shown, the dispersion-dominated case produces wavefront that exhibits the same amplitude as the acoustic case but has a phase delay; the

loss-dominated wavefield has a reduced amplitude but shares the same phase as the acoustic wavefront. Not surprisingly, the viscoacoustic snapshot has the phase of the dispersion-dominated wavefield and the amplitude of the loss-dominated one.

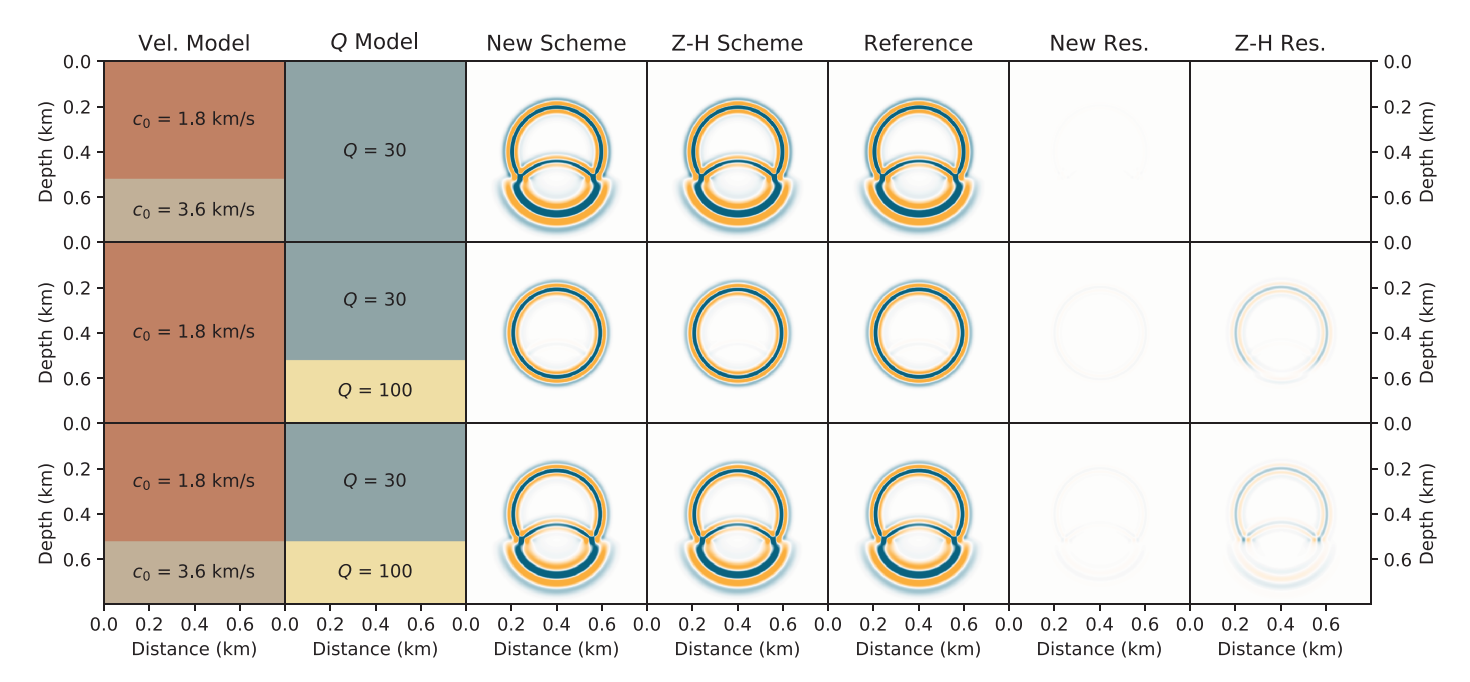


**Figure 6.** Model parameters and wavefield snapshots at 170 ms for the two-layer models. Column 1: velocity model (at 1,500 Hz); column 2: *Q* model; column 3: wavefield snapshots of the simulation using the new scheme in this study; column 4: wavefield snapshots of the simulation using Z-H scheme; column 5: wavefield snapshots of the reference simulation; column 6: residuals between the new scheme and the reference; column 7: residuals between the Z-H scheme and the reference. Row 1: the case with a two-layer velocity model and a homogeneous *Q* model; row 2: the case with a homogeneous velocity model and a two-layer *Q* model; row 3: the case with a two-layer velocity model and a two-layer *Q* model. The color scales are the same for all the snapshots and residuals.

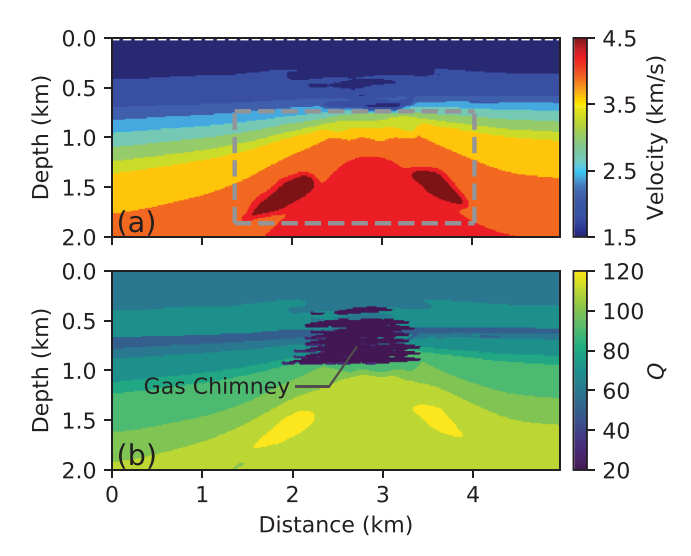


**Figure 7.** The gas chimney model: (a) velocity model at 100 Hz; (b) *Q* model. The white dashed line denotes the depth of the source and the receivers. The gray dashed box is the region whose migration images are shown in Figure 11.

#### 3.2. Two-Layer Model

The two-layer model (Figure 6) is designed to evaluate the simulation accuracy with sharp contrasts. The grid (400 × 400 with 2-m interval), the source location (400 m, 400 m), the wavelet (35-Hz Ricker wavelet), and the time step (0.25 ms) are the same as those in the previous homogeneous example. We run simulations for three different cases: (1) homogeneous Q = 30 with a two-layer velocity model (1,800 m/s for the top and 3,600 m/s for the bottom); (2) homogeneous velocity of 1,800 m/s with a two-layer attenuation model (Q = 30 for the top and Q = 100 for the bottom); (3) two-layer velocity and attenuation model ( $C_0 = 1,800$  m/s,  $C_0 = 30$  for the top and  $C_0 = 3,600$  m/s,  $C_0 = 3,600$  m/s

For each case, we perform the forward modeling using the new scheme in this study as well as the one proposed by Zhu and Harris (2014), that is, equation (1), where the average is taken for the spatially varying  $\gamma$  to implement the fractional Laplacians (hereinafter referred to as Z-H scheme). In addition, we simulate

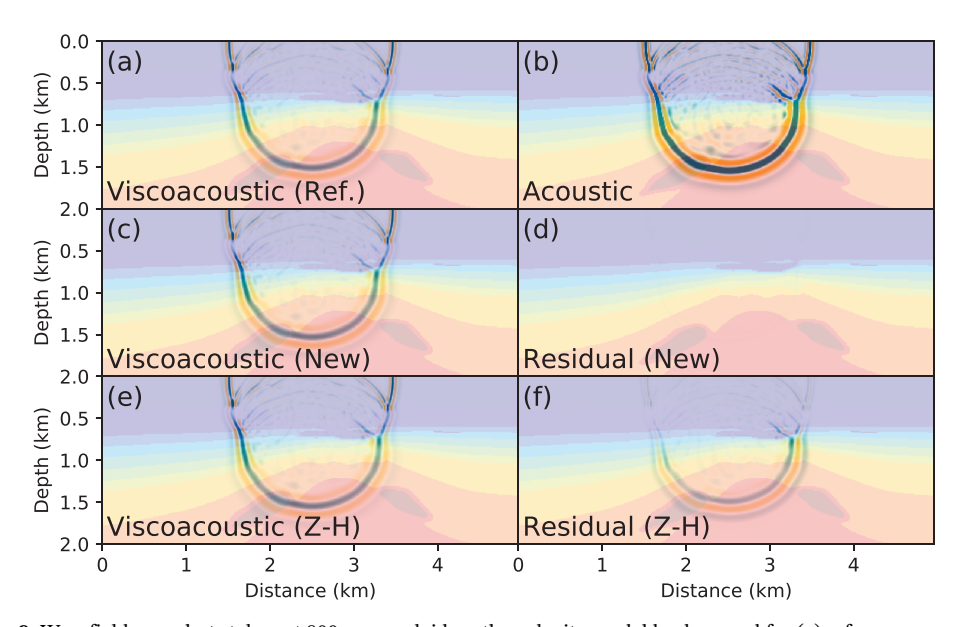


**Figure 8.** Wavefield snapshots taken at 800 ms overlaid on the velocity model background for (a) reference viscoacoustic modeling; (b) acoustic modeling; (c) viscoacoustic modeling with the new scheme; (d) residual between the new scheme and the reference; (e) viscoacoustic modeling with the Z-H scheme; (f) residual between the Z-H scheme and the reference. The color scales are the same for all the snapshots and the residual.

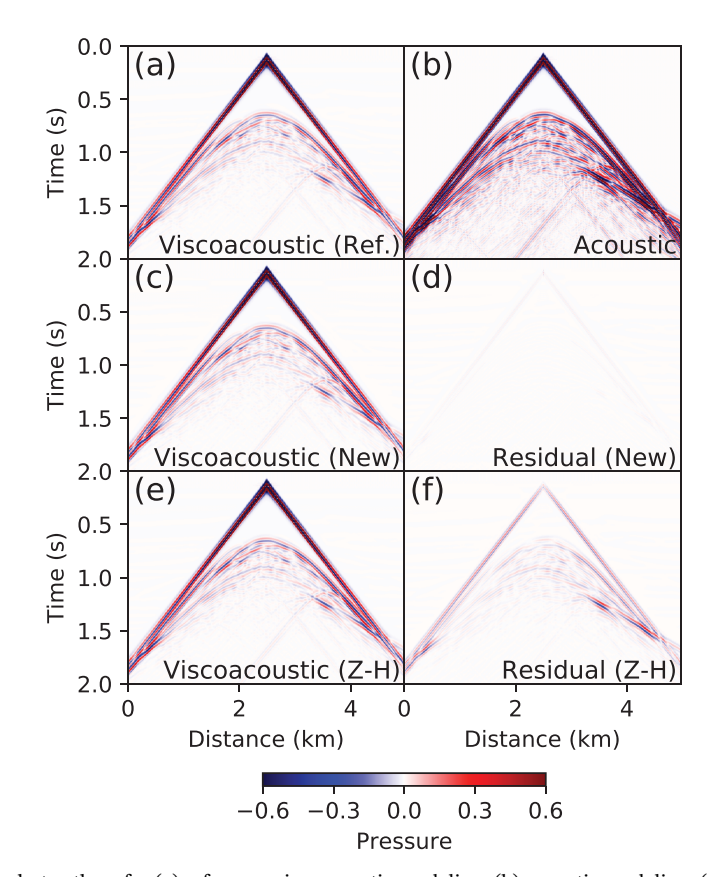


**Figure 9.** Synthetic shot gathers for (a) reference viscoacoustic modeling; (b) acoustic modeling; (c) viscoacoustic modeling with the new scheme; (d) residual between the new scheme and the reference; (e) viscoacoustic modeling with the Z-H scheme; (f) residual between the Z-H scheme and the reference. The color scales are the same for all the shot gathers and the residual.

a reference wavefield, where equation (1) is implemented for each unique Q in the model and the wavefields at different uniform-Q regions are extracted and concatenated together at each time step. In this way, the reference simulation does not suffer from the spatially dependent Q and is accurate although the computational cost is proportional to the number of unique Q values (double for the two-layer Q models). The wavefield snapshots at 170 ms are shown in Figure 6.

In the first case, both schemes match very well with the reference since the Z-H scheme (equation (1)) is essentially as accurate as the new scheme (equation (8)) in a homogeneous Q model. In the second case, the residual for the Z-H scheme is much more significant compared to the one for the new scheme due to their different capabilities of handling heterogeneous Q model. It is worth mentioning that we can observe a weak reflection off the Q interface (around 0.43 km in the second row of Figure 6) although the velocity model is homogeneous. Similarly, the significant residual difference between two schemes in the third case suggest the improved accuracy of our new scheme in dealing with Q contrasts.

# 3.3. Gas Chimney Model and Q-Compensated Reverse Time Migration

In this section, we test our scheme on a highly heterogeneous realistic geological model (Zhu et al., 2014). Figure 7 shows its velocity model at 100 Hz and its Q model. It is a typical model of gas chimney characterized by the low velocity and low-Q zone at the central top. The model is discretized on a  $161 \times 398$  grid with 12.5-m spacing. The source is located in the water layer at (2,500 m, 25 m) with a Ricker wavelet of 15 Hz. The receivers are deployed on all the grid points at the same depth (25 m) as the source and the time step is 1 ms.

We conduct simulations including the acoustic modeling and two viscoacoustic modelings using both the new scheme and the Z-H scheme. Again, we conduct an accurate reference viscoacoustic simulation using the region-wise implementation of equation (1). In this case, the gas chimney Q model consists of 10 regions with unique Q values so the fractional Laplacians are computed separately for each region. The snapshots

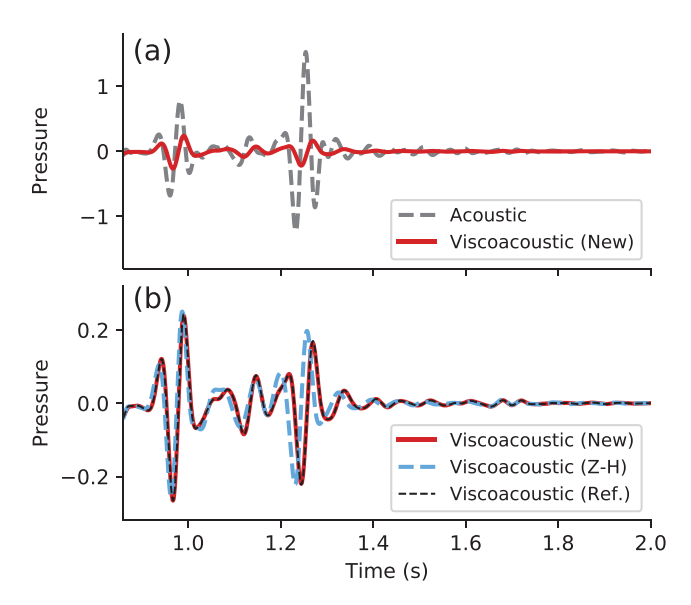


**Figure 10.** Synthetic seismograms (direct arrivals are muted) recorded by the receiver at x = 3,500 m. (a) Comparison between the acoustic modeling (gray dashed line) and the viscoacoustic modeling with the new scheme (red solid line); (b) comparison between viscoacoustic modelings using the new scheme (red solid line), the Z-H scheme (blue dashed line), and the reference (black dashed line).

taken at 800 ms for all the simulations are shown in Figure 8 along with the residuals of the two viscoacoustic schemes compared to the reference. The shot gathers are shown in Figure 9. The synthetics recorded by the receiver at x = 3,500 m are compared with each other as shown in Figure 10 (direct arrivals are muted).

By comparing the acoustic and viscoacoustic modeling, significant amplitude decay can be seen in Figures 8b, 8c, 9b, 9c, and 10a, while the seismogram comparison in Figure 10a exhibits the phase shift. The residual for the new scheme is negligible while that for the Z-H scheme is significant (Figures 8c–8f, 9c–9f, and 10b), which is attributed to their difference in dealing with attenuation heterogeneity. The Z-H scheme adopts average  $\gamma$  in the pseudospectral method to represent the heterogeneous Q distribution, which shows underestimated attenuation for the waves that sample anomalous Q areas, that is, the gas cloud zone in this model. This inference is confirmed by our results (Figure 9f and 10b), as the most significant waveform residuals occur at the reflection phases that sample the gas chimney after 1 s.

In addition to the forward modeling, this new viscoacoustic wave equation can be used to construct the RTM, in particular, the Q-compensated RTM (Q-RTM). The classic RTM image is produced by cross-correlating the forward and backward propagated wavefields produced by acoustic/elastic simulations. The Q-RTM enables mitigating attenuation effects during wavefield simulations to improve the resolution of the seismic images for high-attenuation structures. Following the procedure of the Q-RTM proposed by Zhu et al. (2014), we can build forward and backward compensated wavefields by reversing the signs of the loss correction terms while leaving the signs of the dispersion correction terms unchanged in our new wave equation (equation (8)).

We first generate both the acoustic and the viscoacoustic data sets. Each of them contains shot gathers from 40 sources, which are evenly distributed horizontally at the depth of the receivers (25 m). Thus, example shot gathers of the two data sets can be found in Figures 9a and 9b, respectively, except that the direct waves are muted for the *Q*-RTM implementation. We use a smooth velocity model, which is obtained by processing the true model with a Gaussian filter, to perform three RTMs, that is, the reference case (acoustic RTM on acoustic data set), the noncompensated case (acoustic RTM on viscoacoustic data set), and the compensated case (*Q*-RTM on viscoacoustic data set). For the compensated case, a low-pass Tukey filter with 150 Hz cutoff frequency is applied to suppress the high-frequency noise amplification (Zhu, 2014; Zhu et al., 2014).

The same regions of the resultant seismic images in these three experiments are shown in Figure 11. Compared to the reference image (Figure 11a), the anticline structure beneath the high-attenuation gas chimney is almost invisible in the noncompensated image (Figure 11b) but well illuminated in the compensated case (Figure 11c). Therefore, the new scheme can be utilized to design the Q-RTM to better image subsurface structure of the low Q regions (e.g., gas accumulation in shallow sediments).

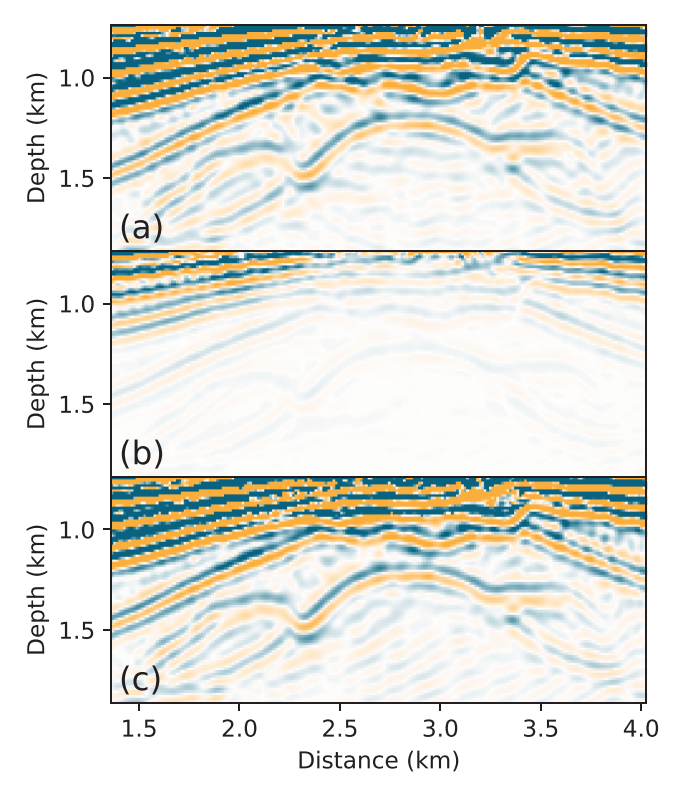


**Figure 11.** Migration images: (a) acoustic reverse time migration (RTM) with acoustic data set; (b) acoustic RTM with viscoacoustic data set; (c) *Q*-RTM with viscoacoustic data set. The range of the region is outlined by the gray dashed lines in Figure 7. The color scales are the same for all the images.

# 3.4. Time-Lapse Seismic Monitoring

In the last example, we model the spatiotemporal attenuation effects on seismic waveforms by performing the time-lapse wavefield simulations in a  $\rm CO_2$  injection geological model derived from the Frio-II brine pilot  $\rm CO_2$  injection experiment (Daley et al., 2007; Zhu et al., 2017, 2019). The time-lapse models of both velocity and Q are retrieved from the Frio-II  $\rm CO_2$  flow simulations using the rocks physics White's model (Daley et al., 2011). We choose three time slices T1 (preinjection baseline), T2 (12 hr after injection), and T3 (48 hr after injection) for wavefield simulations.

The 2-D model has a 434  $\times$  467 grid with 0.15-m spacing. The receiver line with 151 evenly distributed receivers is located in a well, which is 30 m away from the source well (Figure 12). At each time slice, the Q model and the velocity model at a high reference frequency (5 kHz) are shown in Figure 12 and both parameters characterize the evolution of the  $\mathrm{CO}_2$  plume. An 800-Hz Ricker wavelet source is excited at 1,657 m to match the dominant frequency of the Frio-II field data (Daley et al., 2007; Zhu et al., 2017). The simulation time step is 0.02 ms.

For each time slice, we show the wavefield snapshot taken at 16 ms as well as the synthetic shot gather in Figure 13 and the synthetic seismograms recorded by 23 out of 151 receivers in Figure 14a. Compared to the baseline (T1), T2 and T3 waveforms show time-lapse variations because the injected CO<sub>2</sub> progressively replacing the brine in the reservoir modifies the velocity and attenuation structure over time. Meanwhile, the observed spatial variations from the top to the bottom receivers are determined by the CO<sub>2</sub> plume zone.

As shown in Figure 14a, the direct waves of the top few receivers (above  $\sim$ 1,644 m) show consistent waveforms for all the three time slices since their raypaths are not affected by the  $\rm CO_2$  plume (Figures 12c–12h). For these receivers, the subtle deviations of T2 and T3 from the baseline (Figures 13e, 13h, and 14a) are attributed to the interference of the reflection off the plume because the low seismic velocity of the plume enhances the reflections. As the depth increases, the T3 waveforms exhibit significant amplitude decay and phase delay (Figures 13f–13h and 14a) because of the lower velocity and Q inside the  $\rm CO_2$  plume. Such effects are the most significant for the receivers at  $\sim$ 1,650 m, the raypaths of which are influenced the most by the

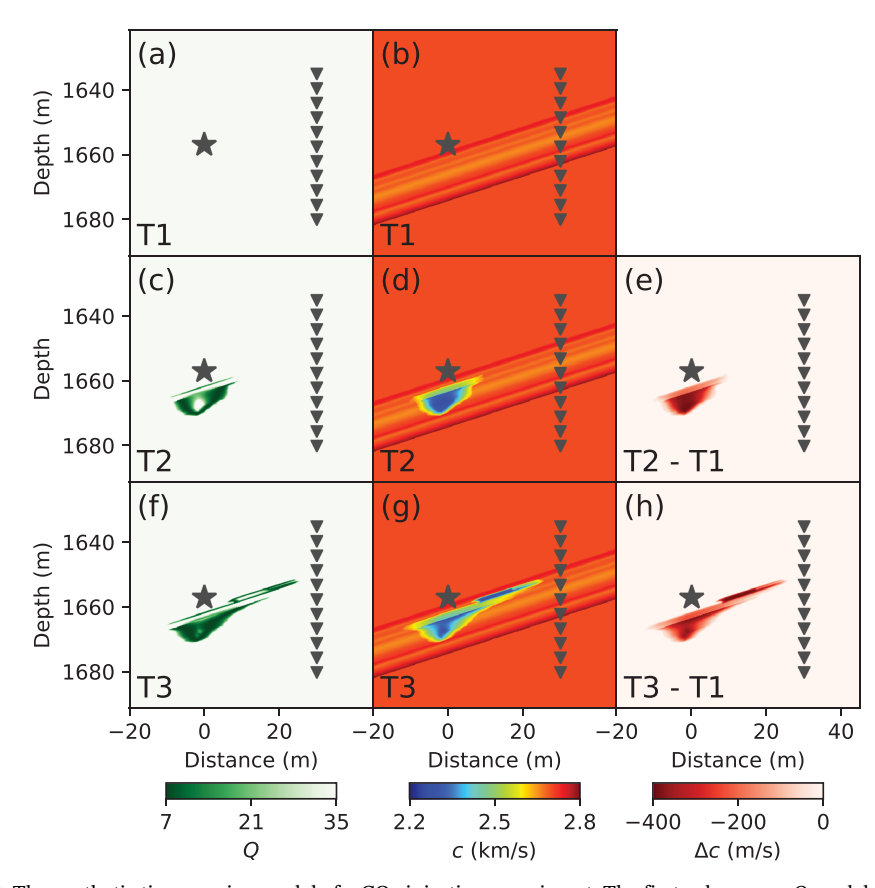


**Figure 12.** The synthetic time-varying model of a  $CO_2$  injection experiment. The first column are Q models for (a) T1 (baseline), (c) T2 (12 hr), and (f) T3 (48 hr) and are saturated on the high-Q end as the media outside the plume area have  $Q \to \infty$ . The second column are the velocity models at 5 kHz for (b) T1, (d) T2, and (g) T3. The third column are the velocity changes relative to the baseline T1 for (e) T2 and (h) T3. The gray star indicates the source location, while the gray triangles indicate the location of the receiver line (11 out of 151 receivers are plotted).

plume (Figures 12f–12h). For the upper middle receivers ( $\sim$ 1,646 to  $\sim$ 1,652 m), the T2 waveforms match the T1 waveforms (Figures 13e and 14a) since the plume has little effect on their raypaths (Figures 12c–12e). In contrast, for the bottom few receivers (below  $\sim$ 1,670 m), the T2 waveforms almost overlap with the T3 waveforms (Figure 14a) because the plume intersecting these raypaths changes very little from T2 to T3 (Figures 12c–12h). For the receivers between these two end-members ( $\sim$ 1,654 to  $\sim$ 1,668 m), the shapes of the T2 waveforms transit progressively from T1 to T3 waveforms (Figure 14a), suggesting the intermediate stage of the CO<sub>2</sub> plume migration.

To calibrate the modeled attenuation effects, we compare the synthetic seismograms with the field data collected at the Frio site. To process the seismic recording at each channel from Zhu et al. (2017), we taper the phases other than the first arrival and shift 1 ms to accommodate the source time function in the numerical modeling, as shown in Figure 14b. Figures 14a and 14b show similar features: the waveforms for all the time slices match fairly well for the top few receivers; T2 and T3 are consistent for the bottom ones with amplitude decay and phase delay compared to T1. To quantify the attenuation effects, we compute the centroid frequency shift (Quan & Harris, 1997) from T1 to T2 and T3 for both synthetic and field data, as shown in Figure 14c. The negative frequency shift is mainly caused by the attenuation effects since the higher-frequency components lose more energy for the waves propagating in frequency-independent Q media while the positive shift is probably due to the interference of later phases. As expected, when direct wave samples the plume, the high-frequency energy is greatly attenuated and the negative frequency shift is observed. This effect is especially significant for T3 at  $\sim$ 1,650 m, where the plume has the most impact on the raypath (Figures 12f–12h). It turns out that the frequency shifts of the synthetic data roughly fit the trend of those from field data. The anomalous positive shifts at the receivers in the middle depth cannot be captured by the seismic modeling. The recordings at these receivers have abnormally high amplitudes

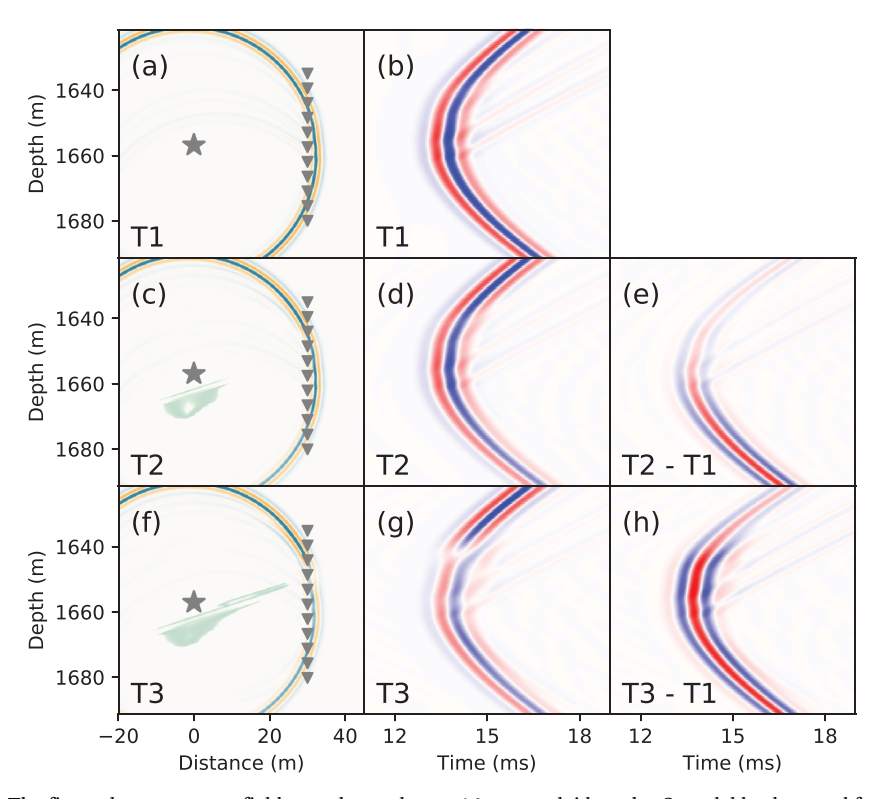


**Figure 13.** The first column are wavefield snapshots taken at 16 ms overlaid on the *Q* model background for different time slices: (a) T1 (baseline), (c) T2 (12 hr), and (f) T3 (48 hr). The second column are synthetic shot gathers for (b) T1, (d) T2, and (g) T3. The third column are the shot gather residuals compared to the baseline T1 for (e) T2 and (h) T3. In the first column, the gray star indicates the source location while the gray triangles indicate the location of the receiver line (11 out of 151 receivers are plotted). All the snapshots have the same color scale; all the shot gathers as well as the residuals also have the same color scale.

(Daley et al., 2011), which implies the inaccuracy of our velocity and attenuation models. We suggest that these waveform anomalies might be generated by the guide waves propagating along the low-velocity zone in the middle of the reservoir (Figure 12b).

# 4. Discussion

Our viscoacoustic wave equation is obtained by adjusting six parameters  $\beta_1, \beta_2, \dots, \beta_6$  to match the six coefficients of x on both sides of equation (6). We found that the last term  $\beta_6$  is negligible as it contains a  $\gamma^4$  factor. Alternatively, we can formulate an overdetermined problem to match the six coefficients by adjusting only five parameters  $\beta_1, \beta_2, \dots, \beta_5$ . It turns out that the least squares solution of this problem is identical to equation (7).

In this framework, more parameters to adjust means more terms in the desired wave equation, which further leads to higher accuracy but a more complicated form of the wave equation thus needs extra computational efforts. In order to achieve a good compromise between accuracy and efficiency, we analyze the scenarios of other parameter selection strategies. Based on the preservation of parameters ( $\beta_1$ ,  $\beta_2$ ,  $\beta_3$ ,  $\beta_4$ ,  $\beta_5$ , and  $\beta_6$ ), we adopt a binary nomenclature. For example, scheme S111110 means using parameters ( $\beta_1$ ,  $\beta_2$ ,  $\beta_3$ ,  $\beta_4$ , and  $\beta_5$ ) without  $\beta_6$ .

Besides scheme S111110 we explore extensively in previous sections, we investigate the performance of schemes S111100, S111010, S011100, and S110100. As in section 2.4, we consider the surface seismic frequency range (10–60 Hz) to validate the phase velocities and the attenuation factors for each scheme against the theoretical solutions for a challenging case where the attenuation is strong (Q=10). Among all the schemes, S011100 and S110100 do not produce stable complex wave number so we restrict our discussion to schemes S111100 and S111010, the results of which are shown in Figure 15.

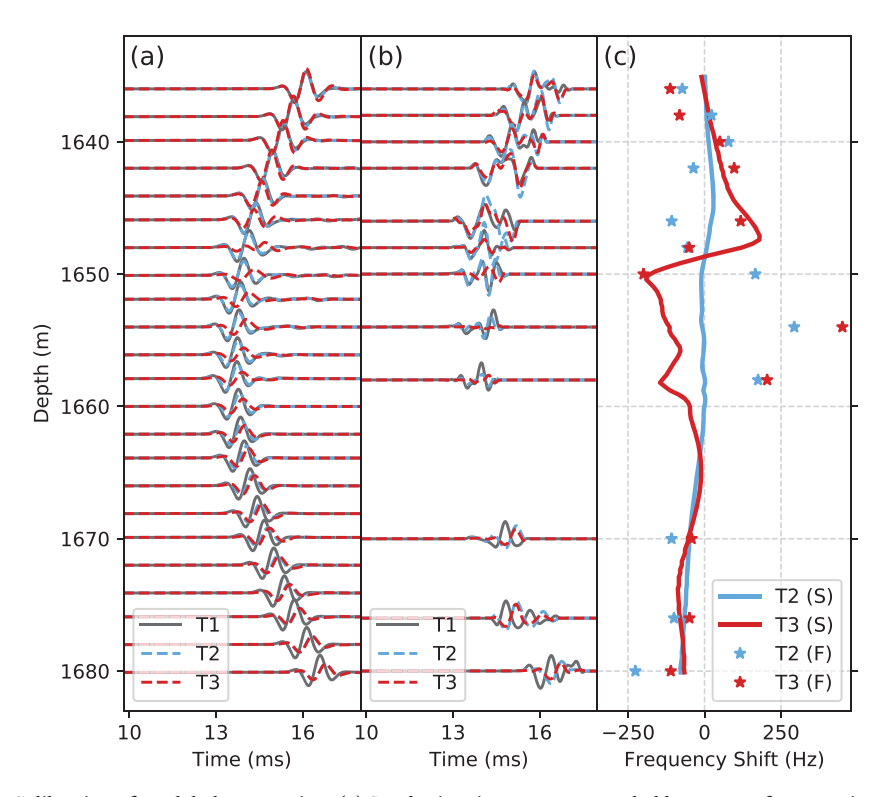


**Figure 14.** Calibration of modeled attenuation. (a) Synthetic seismograms recorded by 23 out of 151 receivers at different depths for time slices T1 (baseline, gray solid lines), T2 (12 hr, blue dashed lines), and T3 (48 hr, red dashed lines). (b) Frio-II field data at different depths for time slices T1 (gray solid lines), T2 (blue dashed lines), and T3 (red dashed lines). The amplitude of each trace in (a) and (b) is normalized according to the baseline recording. (c) Centroid frequency shift compared to T1 for T2 synthetic data (blue solid line), T3 synthetic data (red solid line), T2 field data (blue stars), and T3 field data (red stars).

The comparisons of the dispersion relations show that the S111100 can match both curves fairly well while the S111010 fails to fit the theoretical attenuation factor. Moreover, the parameters of the S111100 turn out to be identical to that of S111110 (equation (7)) except for dropping the term of  $\beta_5$ . The resultant simplified wave equation is

$$\frac{1}{c^2} \frac{\partial^2 p}{\partial t^2} = \nabla^2 p + (\gamma \frac{\omega_0}{c} (-\nabla^2)^{\frac{1}{2}} - \gamma \frac{c}{\omega_0} (-\nabla^2)^{\frac{3}{2}}) p + (-\pi \gamma \frac{1}{c} (-\nabla^2)^{\frac{1}{2}}) \frac{\partial}{\partial t} p.$$
 (14)

Hence, the scheme S111100 can be adopted when the accuracy can be traded for higher efficiency, especially for the scenarios when the *Q* is high.

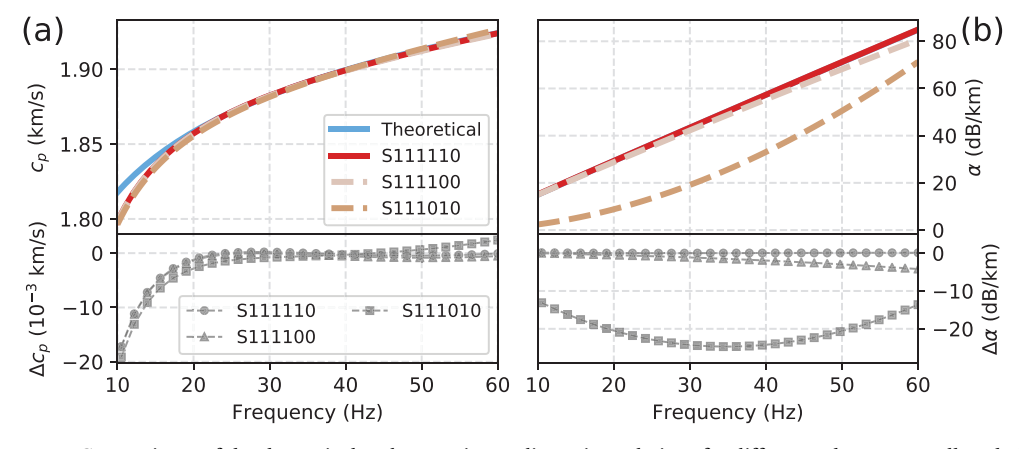


**Figure 15.** Comparisons of the theoretical and approximate dispersion relations for different schemes as well as their residuals: (a) phase velocity; (b) attenuation factor. The legends of (a) also apply to (b).



#### 5. Conclusion

In summary, we have derived a new time-space domain viscoacoustic wave equation based on the frequency-independent Q model. The new equation is favored due to the following reasons. First, it incorporates the spatial fractional Laplacians to avoid the memory issue often encountered by conventional anelastic modeling (e.g., GSLS and fractional time derivative methods). Second, it can accurately handle the heterogeneous Q model as the power terms of the fractional Laplacian operators are independent of the model complexity. Third, this wave equation is able to decouple the two attenuation-associated effects, that is, the amplitude decay and the phase dispersion. The derivation is verified by the comparisons of the resultant dispersion curves with the theoretical ones as well as the in situ measurements. The accuracy of this approximate wave equation is also confirmed by extensive comparisons between the numerical and analytical synthetics in homogeneous models with different Q values. Numerical tests on different realistic geological models suggests that the attenuation effects on waveform amplitude and phase are significant and can be modeled by the proposed wave equation. Moreover, we show that it is straightforward to use the proposed wave equation with decoupled attenuation correction terms to build up the Q-RTM algorithm. We anticipate that the proposed viscoacoustic wave equation having fixed-power fractional Laplacians and explicit Q will directly benefit modeling and imaging applications as well as the development of full waveform Q inversion in seismology.

#### Acknowledgments

This work was supported by the National Energy Technology
Laboratory of the U.S. Department of Energy, under the U.S. DOE Contract
DE-FE0031544 and the NSF Grant
EAR 1919650. All data can be freely accessed on the Energy Data eXchange
(EDX, https://edx.netl.doe.gov/dataset/frio-2-raw-cassm-datasets), operated by the National Energy
Technology Laboratory and utilized under the terms of the Creative
Commons Attribution (CCA) license.

# References

- Adam, L., Batzle, M., Lewallen, K., & van Wijk, K. (2009). Seismic wave attenuation in carbonates. *Journal of Geophysical Research*, 114, B06208. https://doi.org/10.1029/2008JB005890
- Aki, K., & Richards, P. (2002). *Quantitative seismology*. Sausalito, CA: University Science Books. https://books.google.com/books?id=sRhawFG5\_EcC
- Berenger, J. P. (1994). A perfectly matched layer for the absorption of electromagnetic waves. *Journal of computational physics*, 114(2), 185–200.
- Borgomano, J., Pimienta, L., Fortin, J., & Guéguen, Y. (2017). Dispersion and attenuation measurements of the elastic moduli of a dual-porosity limestone. *Journal of Geophysical Research: Solid Earth*, 122, 2690–2711. https://doi.org/10.1002/2016JB013816
- Caputo, M. (1967). Linear models of dissipation whose Q is almost frequency independent-II. *Geophysical Journal International*, 13(5),
- Carcione, J. M. (1999). Staggered mesh for the anisotropic and viscoelastic wave equation. Geophysics, 64(6), 1863-1866.
- Carcione, J. M. (2007). Wave fields in real media: Wave propagation in anisotropic, anelastic, porous and electromagnetic media. Boston, MA: Elsevier Science. Retrieved from https://books.google.com/books?id=tsrwq\_B6HagC
- Carcione, J. M. (2008). Theory and modeling of constant-Q P-and S-waves using fractional time derivatives. Geophysics, 74(1), T1-T11.
- Carcione, J. M. (2010). A generalization of the Fourier pseudospectral method. Geophysics, 75(6), A53-A56.
- Carcione, J. M., Cavallini, F., Mainardi, F., & Hanyga, A. (2002). Time-domain modeling of constant-Q seismic waves using fractional derivatives. *Pure and Applied Geophysics*, 159(7-8), 1719–1736.
- Carcione, J. M., Kosloff, D., & Kosloff, R. (1988). Wave propagation simulation in a linear viscoelastic medium. *Geophysical Journal International*, 95(3), 597–611.
- Chen, W., & Holm, S. (2004). Fractional Laplacian time-space models for linear and nonlinear lossy media exhibiting arbitrary frequency power-law dependency. *The Journal of the Acoustical Society of America*, 115(4), 1424–1430.
- Chen, H., Zhou, H., Li, Q., & Wang, Y. (2016). Two efficient modeling schemes for fractional Laplacian viscoacoustic wave equation. Geophysics, 81(5), T233–T249.
- Daley, T. M., Ajo-Franklin, J. B., & Doughty, C. (2011). Constraining the reservoir model of an injected CO<sub>2</sub> plume with crosswell CASSM at the Frio-II brine pilot. *International Journal of Greenhouse Gas Control*, 5(4), 1022–1030.
- Daley, T. M., Solbau, R. D., Ajo-Franklin, J. B., & Benson, S. M. (2007). Continuous active-source seismic monitoring of CO<sub>2</sub> injection in a brine aquifer. *Geophysics*, 72(5), A57–A61.
- Day, S. M. (1998). Efficient simulation of constant Q using coarse-grained memory variables. *Bulletin of the Seismological Society of America*, 88(4), 1051–1062.
- Duo, S., van Wyk, H. W., & Zhang, Y. (2018). A novel and accurate finite difference method for the fractional Laplacian and the fractional Poisson problem. *Journal of Computational Physics*, 355, 233–252.
- Emmerich, H., & Korn, M. (1987). Incorporation of attenuation into time-domain computations of seismic wave fields. *Geophysics*, 52(9), 1252–1264.
- Fichtner, A., & van Driel, M. (2014). Models and Fréchet kernels for frequency-(in) dependent Q. Geophysical Journal International, 198(3), 1878–1889.
- Guo, P., McMechan, G. A., & Guan, H. (2016). Comparison of two viscoacoustic propagators for *Q*-compensated reverse time migration. *Geophysics*, 81(5), S281–S297.
- Kjartansson, E. (1979). Constant Q-wave propagation and attenuation. Journal of Geophysical Research, 84(B9), 4737-4748.
- Knopoff, L. (1964). Q. Reviews of Geophysics, 2(4), 625-660.
- Liu, H. P., Anderson, D. L., & Kanamori, H. (1976). Velocity dispersion due to anelasticity; implications for seismology and mantle composition. *Geophysical Journal International*, 47(1), 41–58.
- Lu, J. F., & Hanyga, A. (2004). Numerical modelling method for wave propagation in a linear viscoelastic medium with singular memory. Geophysical Journal International, 159(2), 688–702.
- McDonal, F., Angona, F., Mills, R., Sengbush, R., Van Nostrand, R., & White, J. (1958). Attenuation of shear and compressional waves in Pierre Shale. *Geophysics*, 23(3), 421–439.



- Meurer, A., Smith, C. P., Paprocki, M., Čertík, O., Kirpichev, S. B., Rocklin, M., & Scopatz, A. (2017). SymPy: Symbolic computing in Python. PeerJ Computer Science, 3, e103. https://doi.org/10.7717/peerj-cs.103
- Moczo, P., & Kristek, J. (2005). On the rheological models used for time-domain methods of seismic wave propagation. *Geophysical Research Letters*, 32, L01306. https://doi.org/10.1029/2004gl021598
- Molyneux, J. B., & Schmitt, D. R. (2000). Compressional-wave velocities in attenuating media: A laboratory physical model study. *Geophysics*, 65(4), 1162–1167.
- Müller, T. M., Gurevich, B., & Lebedev, M. (2010). Seismic wave attenuation and dispersion resulting from wave-induced flow in porous rocks- A review. *Geophysics*, 75(5), 75A147–75A164.
- Operto, S., Virieux, J., Amestoy, P., L'Excellent, J. Y., Giraud, L., & Ali, H. B. H. (2007). 3D finite-difference frequency-domain modeling of visco-acoustic wave propagation using a massively parallel direct solver: A feasibility study. *Geophysics*, 72(5), SM195–SM211.
- Peters, L., Anandakrishnan, S., Alley, R., & Voigt, D. (2012). Seismic attenuation in glacial ice: A proxy for englacial temperature. *Journal of Geophysical Research*, 117, F02008. https://doi.org/10.1029/2011JF002201
- Quan, Y., & Harris, J. M. (1997). Seismic attenuation tomography using the frequency shift method. Geophysics, 62(3), 895-905.
- Robertsson, J. O., Blanch, J. O., & Symes, W. W. (1994). Viscoelastic finite-difference modeling. Geophysics, 59(9), 1444-1456.
- Romanowicz, B. (1995). A global tomographic model of shear attenuation in the upper mantle. *Journal of Geophysical Research*, 100(B7), 12,375–12,394.
- Sams, M., Neep, J., Worthington, M., & King, M. (1997). The measurement of velocity dispersion and frequency-dependent intrinsic attenuation in sedimentary rocks. *Geophysics*, 62(5), 1456–1464.
- Shen, Y., & Zhu, T. (2015). Image-based *Q* tomography using reverse time *Q* migration, *SEG Technical Program Expanded Abstracts 2015* (pp. 3694–3698). Tulsa, OK: Society of Exploration Geophysicists.
- Sun, J., Fomel, S., Zhu, T., & Hu, J. (2016). Q-compensated least-squares reverse time migration using low-rank one-step wave extrapolation. Geophysics, 81(4), S271–S279.
- Sun, J., Zhu, T., & Fomel, S. (2015). Viscoacoustic modeling and imaging using low-rank approximation. *Geophysics*, 80(5), A103–A108. Treeby, B. E., & Cox, B. (2010). Modeling power law absorption and dispersion for acoustic propagation using the fractional Laplacian. *The Journal of the Acoustical Society of America*, 127(5), 2741–2748.
- van Driel, M., & Nissen-Meyer, T. (2014). Optimized viscoelastic wave propagation for weakly dissipative media. *Geophysical Journal International*, 199(2), 1078–1093.
- Waters, K. R., Mobley, J., & Miller, J. G. (2005). Causality-imposed (Kramers-Kronig) relationships between attenuation and dispersion. IEEE transactions on ultrasonics, ferroelectrics, and frequency control, 52(5), 822–823.
- Wiens, D. A., Conder, J. A., & Faul, U. H. (2008). The seismic structure and dynamics of the mantle wedge. *Annual Review of Earth and Planetary Sciences*. 36. 421–455.
- Wuenschel, P. C. (1965). Dispersive body waves—An experimental study. Geophysics, 30(4), 539-551.
- Xue, Z., Sun, J., Fomel, S., & Zhu, T. (2017). Accelerating full-waveform inversion with attenuation compensation. *Geophysics*, 83(1), A13–A20.
- Yang, J., & Zhu, H. (2018). Viscoacoustic reverse time migration using a time-domain complex-valued wave equation. Geophysics, 83(6), S505–S519.
- Yao, J., Zhu, T., Hussain, F., & Kouri, D. J. (2016). Locally solving fractional Laplacian viscoacoustic wave equation using Hermite distributed approximating functional method. Geophysics, 82(2), T59–T67.
- Zhu, T. (2014). Time-reverse modelling of acoustic wave propagation in attenuating media. *Geophysical Journal International*, 197(1),
- Zhu, T. (2017). Numerical simulation of seismic wave propagation in viscoelastic-anisotropic media using frequency-independent Q wave equation. *Geophysics*, 82(4), WA1–WA10.
- Zhu, T., Ajo-Franklin, J. B., & Daley, T. M. (2017). Spatiotemporal changes of seismic attenuation caused by injected CO<sub>2</sub> at the Frio-II pilot site, Dayton, TX, USA. *Journal of Geophysical Research: Solid Earth*, 122, 7156–7171. https://doi.org/10.1002/2017JB014164
- Zhu, T., Ajo-Franklin, J., Daley, T. M., & Marone, C. (2019). Dynamics of geologic CO<sub>2</sub> storage and plume motion revealed by seismic coda waves. Proceedings of the National Academy of Sciences, 116(7), 2464–2469.
- Zhu, T., Carcione, J. M., & Harris, J. M. (2013). Approximating constant-Q seismic propagation in the time domain. *Geophysical Prospecting*, 61(5), 931–940.
- Zhu, T., & Harris, J. M. (2014). Modeling acoustic wave propagation in heterogeneous attenuating media using decoupled fractional Laplacians. *Geophysics*, 79(3), T105–T116.
- Zhu, T., Harris, J. M., & Biondi, B. (2014). Q-compensated reverse-time migration. Geophysics, 79(3), S77-S87.
- Zhu, T., & Sun, J. (2017). Viscoelastic reverse time migration with attenuation compensation. Geophysics, 82(2), S61-S73.
- Štekl, I., & Pratt, R. G. (1998). Accurate viscoelastic modeling by frequency-domain finite differences using rotated operators. *Geophysics*, 63(5), 1779–1794.